First-order finite-Larmor-radius effects on magnetic tearing in pinch configurations

J. R. King, C. R. Sovinec, and V. V. Mirnov

Citation: Phys. Plasmas **18**, 042303 (2011); doi: 10.1063/1.3571599
View online: http://dx.doi.org/10.1063/1.3571599
View Table of Contents: http://pop.aip.org/resource/1/PHPAEN/v18/i4
Published by the American Institute of Physics.

First-order finite-Larmor-radius effects on magnetic tearing in pinch configurations

J. R. King,[1,2,a)] C. R. Sovinec,[1,3] and V. V. Mirnov[1,2]
[1]*Center for Magnetic Self-Organization and Center for Plasma Theory and Computation, 1150 University Avenue, Madison, Wisconsin 53706, USA*
[2]*Department of Physics, University of Wisconsin-Madison, 1150 University Avenue, Madison, Wisconsin 53706, USA*
[3]*Department of Engineering-Physics, University of Wisconsin-Madison, 1500 Engineering Drive, Madison, Wisconsin 53706, USA*

(Received 21 December 2010; accepted 10 March 2011; published online 22 April 2011)

The linear and nonlinear evolution of a single-helicity tearing mode in a cylindrical, force-free pinch are investigated using a fluid model with first-order finite-Larmor-radius corrections. Linear results computed with the NIMROD [nonideal magnetohydrodynamics (MHD) with rotation, open discussion] code [Sovinec *et al.*, J. Comput. Phys. **195**, 355 (2004)] produce a regime at small ρ_s where the growth rate is reduced relative to resistive MHD, though the Hall term is not significant. The leading order contributions from ion gyroviscosity may be expressed as a drift associated with ∇B_0 and poloidal curvature for experimentally relevant $\beta = 0.1$, $S \sim 10^5 - 10^6$ force-free equilibria. The heuristic analytical dispersion relation, $\gamma^4(\gamma - i\omega_{*gv}) = \gamma^5_{MHD}$ where ω_{*gv} is the gyroviscous drift frequency, confirms numerical results. The behavior of our cylindrical computations at large ρ_s corroborates previous analytic slab studies where an enhanced growth rate and radially localized Hall dynamo are predicted. Similar to previous drift-tearing results, nonlinear computations with cold ions demonstrate that the Hall dynamo is small when the island width is large in comparison with the scale for electron–ion coupling. The saturation is then determined by the resistive MHD physics. However, with warm ions the gyroviscous stress supplements the nonlinear Lorentz force, and the saturated island width is reduced. © *2011 American Institute of Physics*. [doi:10.1063/1.3571599]

I. INTRODUCTION

Standard operation of reversed-field pinch (RFP) experiments relies on macroscopic magnetohydrodynamic-like modes to distribute the parallel component of the current density over the profile. The resulting broad distribution gives the configuration its characteristic reversal of the toroidal magnetic field near the wall. With some possible exceptions, the dominant unstable modes of standard RFP profiles are tearing modes[1] that saturate nonlinearly by coupling to stable resonant modes[2] and by reducing their drive through profile modification.[3] Mean-field analysis[4] for fluid models shows that part of the parallel-current-density profile can be sustained against resistive dissipation by an electromotive force (emf) produced from the correlation of fluctuations. In single-fluid models, the correlation of fluctuating flows and magnetic field induces the MHD dynamo effect.[5] Two-fluid models allow a Hall dynamo effect from the correlation of the fluctuating current density and magnetic field,[6,7] in addition to the MHD dynamo effect. Laser polarimetry measurements in the Madison Symmetric Torus (MST, see Ref. 8) RFP show that the Hall dynamo effect is very important during the intermittent relaxation events known as RFP "sawteeth."[9,10] To provide a basis for understanding two-fluid effects in MST, the computations presented here consider linear and nonlinear properties of individual tearing modes in cylindrical pinch profiles with uniform density and temperature. These equilibrium conditions approximate the core of relaxed pinches that largely confine particles and energy in their outer region.

In the parameter regimes of interest, important non-MHD effects arise from particle motions as finite-Larmor-radius (FLR) contributions. For example, in the MST discharges described in Ref. 9, the ion-sound gyroradius is approximately 1 cm, less than a tenth of the minor radius but also larger than a tearing layer width. The FLR effects may be included in a fluid model, to first order, with a two-fluid Ohm's law and ion gyroviscosity. Their influence on tearing modes has been the subject of many theoretical studies over more than four decades. A review is beyond the scope of this paper, but the most relevant previous work begins with Coppi's analysis of ion FLR effects, which identifies drift-tearing behavior resulting from pressure gradients at the resonant surface.[11] This study ordered both the pressure and the reconnecting component of magnetic field to be small, as appropriate for large-aspect ratio tokamaks. A linear stabilization effect from warm ions in the computations presented here is similar to Coppi's analysis. However, our computations do not consider equilibrium diamagnetic flow, and the drift effect arises from poloidal curvature and the gradient of the magnitude of the equilibrium magnetic field, both of which are important in RFPs.

Regarding the magnetic-field evolution, Drake and Lee identified the importance of electron responses to the parallel component of the perturbed electric field in collisionless and semi-collisional regimes that occur when the

a)Electronic mail: jacobrking@gmail.com.

reconnection scale is smaller than the ion gyroradius.[12] Their discussion emphasizes competition between parallel electron acceleration, magnetic shear that limits the spatial scale of acceleration, electron–ion collisions that impede acceleration and broaden the layer, and ion perpendicular drifts at radial scales where the ions are magnetized. That the separation of the electron and ion responses is not specifically dependent on ion thermal energy but also arises at scales below ρ_s from electron thermal energy was emphasized in Ref. 13 for the $m=1$ tokamak mode. This type of separation is discussed in general terms for reconnection in Ref. 14 as a kinetic-Alfvén-wave (KAW) type dispersive response that maintains reconnection outflows at scales below ρ_s. A limitation on the electron response due to diffusion of the perturbed magnetic field that is parallel to the guide field at large plasma-β is identified in Ref. 15. The relations among different limits of two-fluid reconnection with respect to β and the tearing stability parameter Δ' for slab equilibria with uniform pressure are also described. These results were made yet more general to include the MHD regime in Ref. 16 by assuming minimal values of β.

The linear computations presented here confirm that electron-fluid separation increases tearing growth rates in cylindrical pinch profiles when ρ_s exceeds the resistive skin depth. In addition, our computations that include warm-ion effects through fluid gyroviscosity show an intermediate drift-regime with reduced growth rates at ρ_s-values that are smaller than the resistive skin depth. In warm-ion conditions where ρ_s is comparable to the resistive skin depth, the electron dynamics are decoupled, and the tearing mode becomes less sensitive to the ion dynamics. Thus, first-order FLR modeling for warm ions should provide at least a semi-quantitative description of tearing through the transition from MHD to electron-MHD.

Our nonlinear two-fluid computations with cold ions show magnetic islands that evolve to the same saturated width found with resistive MHD modeling. This is expected from early nonlinear results on drift-tearing modes that apply large-aspect ratio tokamak ordering. In particular, Refs. 17 and 18 include fluid gyroviscous effects where the dominant contribution is related to the ion pressure gradient. In Ref. 17, a quasilinear mixing-length argument is applied to justify an assumption of particle density and ion temperature flattening over magnetic island flux surfaces, which leads to resistive-MHD evolution at finite island width in quasilinear computation. In Ref. 18, density is not assumed to flatten over the evolving island in nonlinear computations. While this affects rotation during the evolution, the helical flux evolution is shown to be independent of rotation, and the saturated state again matches resistive MHD predictions. More complete nonlinear modeling confirms the density-flattening effect through sound-wave mixing.[19]

In contrast, our computations with warm ions show that the ion-gyroviscous stress in pinch configurations affects nonlinear island evolution and saturation. The gyroviscous stress supplements the nonlinear Lorentz force[20] that occurs in resistive MHD and reduces saturated island widths. Moreover, the magnetic curvature and the gyrofrequency profile, which lead to the important gyroviscous contributions in pinch profiles, are largely unaffected by the nonlinear evolution, unlike the pressure-gradient effects considered in other studies. Perpendicular current density and the Hall dynamo effect are, therefore, nonzero at saturation. Our computations do not consider thermal conduction effects. The spatial scale of the temperature profile is larger than the magnetic shear scale in the core of standard RFPs, which reduces the importance of thermal conduction linearly[21] and for small perturbations.[22] In addition, temperature profile effects are not important for large nonlinear perturbations,[22] and large perturbations occur in the RFP.

In standard RFP discharges, the confinement time is primarily limited by the magnetic islands overlapping which produces a stochastic magnetic topology, and particles and energy are poorly confined along radially wandering field-lines. However, magnetic self-organization leads to improved confinement in quasi-single-helicity (QSH) states where magnetic perturbations of a single-helicity dominate.[23] Additionally, significant progress has been made though RFP profile control, whereby the free energy available to the instabilities and ultimately the island sizes are limited and the confinement is greatly improved compared to traditional RFP scaling.[24] Although our studies of single tearing-mode dynamics are not directly applicable to inherently multimode discharges, a clear understanding of the physics governing the mode growth rate and island saturation width is essential in order to characterize the tearing activity in RFPs. How the two-fluid effects studied here may influence the performance of QSH and profile-control experiments is considered in the conclusions.

The remainder of this paper is organized as follows. In Sec. II, we describe our two-fluid model that includes a generalized Ohm's law and ion gyroviscosity in a system for the evolution of particle density, center of mass flow velocity, temperature, and magnetic field. In Sec. III, we describe the equilibrium profiles, physical parameters, and the numerical implementation. Our linear computations are presented in Sec. IV with analysis of the gyroviscous contribution and evaluation of linear dynamo effects for comparison with previous studies. Results on the saturated island width and the nonlinear gyroviscous force are described in Sec. V. Our conclusions regarding single-helicity tearing are given in Sec. VI, followed by additional information on the analysis of linear gyroviscous effects in the Appendix.

II. TWO-FLUID MODELING

For readability, we define all quantities before proceeding. Following convention, **B** and **E** are the magnetic and electric fields, respectively, and **J** is the current density. We denote the center of mass flow velocity as **v**, and n, $p=p_e+p_i$, and $T_{e/i}$ are the density, pressure, and species temperature, respectively. The subscript "i" indicates an ion-species quantity, and the subscript "e" indicates the electron species. The ideal gas law relates the pressure and temperature for each species, $p_\alpha = nk_BT_\alpha$. We use $\eta/\mu_0, D_n, \nu$, and χ for the magnetic, particle, viscous, and thermal diffusivities, respectively. Finally, m_e is the electron mass, e is the elementary charge, k_B is the Boltzmann constant, and Γ is the ratio of specific heats.

Our two-fluid model uses Faraday's law, $\partial \mathbf{B}/\partial t = -\nabla \times \mathbf{E}$, and Ampere's law without displacement current, $\mu_0 \mathbf{J} = \nabla \times \mathbf{B}$, as appropriate for low frequency dynamics. We assume quasineutrality and solve the electron momentum equation for the electric field to produce a generalized Ohm's law,

$$\mathbf{E} = -\mathbf{v} \times \mathbf{B} + \frac{\mathbf{J} \times \mathbf{B}}{ne} - \frac{\nabla p_e}{ne} + \eta \mathbf{J} + \frac{m_e}{ne^2}\frac{\partial \mathbf{J}}{\partial t}, \quad (1)$$

where the first and second terms on the right-hand side (RHS) are the ideal-MHD and Hall contributions. From the definition of current density, $\mathbf{v}_e = \mathbf{v}_i - \mathbf{J}/ne$, and with $\mathbf{v} \cong \mathbf{v}_i$, the combination of the first two terms is equivalent to $-\mathbf{v}_e \times \mathbf{B}$. When $\mathbf{J}/ne$ is large in comparison with v_i, it signifies decoupling of the electron and ion fluids. To the extent that the last three terms of Eq. (1) are small, $\mathbf{E} \cong -\mathbf{v}_e \times \mathbf{B}$, and the magnetic flux is frozen into the electron fluid.

The continuity, momentum, and energy equations describe the temporal evolution of the density, center of mass fluid velocity, and temperature,

$$\frac{dn}{dt} = -n\nabla \cdot \mathbf{v} + D_n \nabla^2 n, \quad (2)$$

$$m_i n \frac{d\mathbf{v}}{dt} = \mathbf{J} \times \mathbf{B} - \nabla p - \nabla \cdot \mathbf{\Pi}_{gyro} - \nabla \cdot \nu m_i n \mathbf{W}, \quad (3)$$

$$\frac{n}{\Gamma - 1}\frac{dT}{dt} = -p\nabla \cdot \mathbf{v} + \nabla \cdot \chi n \nabla T, \quad (4)$$

using the total time-derivative $d/dt \equiv \partial/\partial t + \mathbf{v} \cdot \nabla$. We model the electron and ion temperatures as remaining at a fixed fractions of T, i.e., $T_i = f_{Ti} T$ and $T_e = (1 - f_{Ti})T$, where f_{Ti} is a specified parameter. Separate sets of computations reported in Secs. IV and V consider the cold-ion ($f_{Ti} = 0$) and rapid-equilibration ($f_{Ti} = 0.5$) limits. The last terms on the RHS of Eqs. (2)–(4) are diffusive terms included for numerical stability. In cases presented here, their coefficients are chosen to be small with respect to resistivity, such that the magnetic Prandtl number, $P_m = \mu_0 \nu/\eta = 0.1$, and $D_n = \chi = \nu$. Note that with uniform equilibrium temperature, we do not include realistic thermal conduction effects in the present work. The force from the ion-gyroviscous stress is the second to last term on the RHS of Eq. (3). It represents gyro-orbit frequency shifts and ellipticity resulting from $\nabla \mathbf{E}$ and is nondissipative.[25] The gyroviscous stress derived for a collisional plasma in the small ion gyroradius (ρ_i) limit[26] is

$$\mathbf{\Pi}_{gyro} = \frac{m_i p_i}{4eB}\left[\hat{\mathbf{b}} \times \mathbf{W} \cdot \left(\mathbf{I} + 3\hat{\mathbf{b}}\hat{\mathbf{b}}\right) - \left(\mathbf{I} + 3\hat{\mathbf{b}}\hat{\mathbf{b}}\right) \cdot \mathbf{W} \times \hat{\mathbf{b}}\right], \quad (5)$$

where $\mathbf{W} = \nabla \mathbf{v} + \nabla \mathbf{v}^T - (2/3)\mathbf{I}\nabla \cdot \mathbf{v}$ is the rate of strain tensor, and $\hat{\mathbf{b}}$ is the unit direction vector for an arbitrarily oriented magnetic field. For flows of the order of the ion thermal speed, the gyroviscous force scales as ρ_i/L times the pressure-gradient force, where $\rho_i = v_{Ti}/\omega_{ci}$, L is a characteristic gradient length, $v_{Ti} = \sqrt{k_B T_i/m_i}$, and $\omega_{ci} = eB/m_i$. Therefore, the force is important with warm ions.

After prescribing the relation among diffusion coefficients, a set of five dimensionless parameters describes the plasma in our model: (1) f_{Ti}, (2) the plasma-β ($2\mu_0 p/B_0$), (3) and (4) the normalized ion and electron skin depths, $d_\alpha/a = c/\omega_{p\alpha}a$, where $\omega_{p\alpha} = \sqrt{ne^2/\epsilon_0 m_\alpha}$ is the plasma frequency for species α and a is the minor radius, and (5) the Lundquist number, $S = \tau_R/\tau_A$, where $\tau_R = \mu_0 a^2/\eta$ is the resistive time and $\tau_A = a/v_A = a\sqrt{\mu_0 \rho_0}/B_0$ is the Alfvén time. In experiment, the ion and electron skin depths are not independent, as their ratio is determined by the electron and ion masses.

In the MST discharges analyzed in Ref. 9, the electron and ion temperatures are approximately 300 eV, $n \simeq 10^{19}\mathrm{m}^{-3}$, $B \simeq 0.4T$, the minor radius is $a \simeq 0.5$ m, and the major radius is $R \simeq 1.5$ m. The ion sound gyroradius is evaluated as $\rho_s = c_s/\omega_{ci} = \sqrt{\Gamma\beta/2}d_i$, where the sound speed is $c_s = \sqrt{\Gamma k_B(T_i + T_e)/m_i}$, and the MST conditions have $d_i \simeq 0.2a$ and $\rho_s \simeq 0.02a$. Using linear growth rates reported here to estimate the resistive skin depth, $\delta = \sqrt{1/\gamma\tau_A S}$, in the MST discharges shows that $\delta \simeq \rho_s$ for core modes in an unrelaxed current profile. In more relaxed profiles, the growth rate is smaller, which would put the linear behavior more in the MHD regime. However, nonlinearly driven modes may grow faster and have skin depths that are significantly smaller than ρ_s; though, semi-collisional ($\delta >> d_e$) conditions[12,27] are still expected. Understanding the transition from MHD to two-fluid tearing is therefore important for MST. From the discussion in Ref. 15, we also find that conditions for the linear behavior are in the transition region from small to large stability-parameter, as measured by $\Delta'\delta$. Here, we examine the two-fluid transition by varying d_i hence ρ_s while keeping β, S, and Δ' fixed so that the MHD response does not change for a given S-value. Our linear computations have $S = 8 \times 10^4$ or 1×10^6, while in MST, $S \simeq 8 \times 10^6 Z^{-1}$, where Z is the effective ion charge number, which is at least 2. Our nonlinear pinch computations have the same low P_m-value of 0.1, and computational practicalities presently limit them to $S \lesssim 1 \times 10^5$.

III. METHODS AND PARAMETERS

A. Numerical methods

We solve Eqs. (2)–(4) plus Faraday's law with the generalized Ohm's law, Eq. (1), using the initial-value, extended-MHD NIMROD (nonideal MHD with rotation, open discussion) code.[28] The implementation evolves perturbations from a prescribed steady equilibrium, and the computations may be either linear or fully nonlinear. Results on pinch tearing modes reported in Sec. IV are computed with the linear option. In Sec. V, we describe results from fully nonlinear computations, including modification of the symmetric profiles. The two-fluid implicit leap-frog time-advance has been benchmarked with analytic tearing results in slab geometry without ion gyroviscosity and on plane-wave propagation and slab interchange with ion gyroviscosity.[29,30]

The code's spatial representation is spectral finite elements over a two-dimensional plane and finite Fourier series for a periodic coordinate. In the cylindrical-pinch computations described here, we use the Fourier representation for the azimuthal angle and the finite-element representation for

the rz plane. We impose periodic boundary conditions in the axial direction of the cylinder, with periodicity $2\pi R$. Most of our nonlinear computations have $0 \leq m \leq 2$ Fourier components and finite-element basis functions of polynomial degree four in a 240×30 (*radial* $\times$ *axial*) mesh that is packed about the rational surface. Numerical convergence has been checked by running computations with polynomial basis functions of degree five and six Fourier components, $0 \leq m \leq 5$. Apart from an effective axial voltage, boundary conditions in the computations represent a conducting wall with no-slip conditions on flow at $r = a$. Dirichlet conditions are also used for the evolving number density and temperature. Edge-peaked profiles for the resistivity and isotropic viscosity increase by a factor of 10 or 20 and spread boundary-layer effects over a narrow region adjacent to the wall.

B. Equilibrium configuration

Our computations use the force-free ($\mathbf{J}_{eq} \times \mathbf{B}_{eq} = \nabla p_{eq} = 0$), cylindrical, paramagnetic-pinch equilibrium[31] with $p_{eq} \neq 0$ to investigate finite-β two-fluid effects without equilibrium diamagnetic flow. Effects from nonzero equilibrium ω_{*i} are left for future work. We include a radial pinch flow, $\mathbf{v}_{eq} = \mathbf{E}_{eq} \times \mathbf{B}_{eq}/\mathbf{B}_{eq}^2$ such that $\nabla \times \mathbf{E}_{eq} = 0$ with uniform axial electric field, so the equilibrium is an Ohmic steady state. The particle and energy compression from $\nabla \cdot \mathbf{v}_{eq}$ are not considered in these simulations; we assume that they are balanced by transport processes that are outside the scope of the model. Moreover, the pinch flow scales as $1/S$, and in the experimentally relevant high-S regime, it is likely to be just a small part of overall transport. The parallel-current profile, $\lambda(r) = a\mu_0 \mathbf{J}_0 \cdot \mathbf{B}_0/\mathbf{B}_0^2$ has $\lambda(0) = 3.3$ in the computations discussed here. This results in a pinch parameter value of $\Theta = \mathbf{B}_{\theta 0}(a)/\overline{\mathbf{B}_{z0}} = 1.38$, where the overbar indicates the volume average. The equilibrium parallel-current profile is shown in Fig. 1(a). This pinch-parameter value is roughly 10%–15% below that of the MST discharges described in Ref. 9. At larger pinch parameter values, the parallel-current-density gradients of the paramagnetic pinch are larger, which is less representative of relaxed RFP profiles.

We limit the fluctuation spectrum of our nonlinear computations, which are three-dimensional, by using a reduced aspect ratio of $R/a = 0.505$. This value makes the first axial wavenumber, $k_z a = 1.98$, comparable to that of the dominant $m = 1$, $n = 6$ mode in MST. The safety factor [$q(r) = rB_{z0}/RB_{\theta 0}$ in a cylinder] for the computations is shown in Fig. 1(b), and the primary mode is resonant at the $q = 1$ rational surface, $r_s = 0.35$. Unlike MST, however, the next axial wavenumber is twice as large as that of the dominant mode, which limits nonlinear coupling and allows us to focus on single-helicity behavior in this study. The dominant $m = 1$, $k_z a = 1.98$ mode in the computations has the tearing stability parameter $\Delta' a = 15.2$, according to an independent eigenvalue computation for tearing modes. The only other MHD-unstable mode for this equilibrium has $m = 1$ and $k_z a = 3.96$. Its stability parameter value of $\Delta' a = 3.0$ leads to a smaller resistive-MHD growth rate, and the stabilizing gyroviscous effect described in Sec. IV is considerably stronger for this mode. It is not observed to be significant in our nonlinear computations. Our computations allow the dominant mode to couple with its higher harmonics, $m = 2, 3, \ldots$, so single-helicity shaping and spectral broadening are permitted numerically, but these effects are not observed to be significant for these cases. Finally, we note that the paramagnetic pinch is not a reversed state; reversal is achieved via the full RFP dynamo, which is not present in these low-Θ, reduced aspect ratio cases.

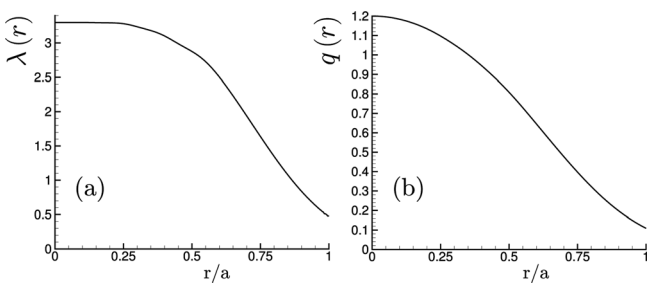

FIG. 1. The (a) parallel-current profile and (b) safety factor vs radius for the paramagnetic pinch with $\lambda_0 = 3.3$ and $R/a = 0.505$.

C. Parameter scans

Summarizing the parameters used in our computations, the cylindrical geometry has $R/a = 0.505$, the force-free equilibrium has $\lambda(0) = 3.3$, and we set $\beta = 0.1$. In our linear computations, we vary d_i/a from very small values to larger than unity, to cover the transition from resistive-MHD to electron-MHD. The Lundquist number, S, in the linear computations reported here is either 8×10^4 or 1×10^6. For convenience, the electron mass is artificially increased by a factor of 10 in most computations relative to the physical value, thus the mass ratio is $m_e/m_i = 2.72 \times 10^{-3}$, and the ratio of the skin depths is $d_e/d_i = 5.21 \times 10^{-2}$. Computations near the electron-MHD limit have more realistic mass ratios such that $d_e = \min(5.21 \times 10^{-2} d_i,\ 9.0 \times 10^{-3} a)$, so that all tearing conditions are in the semi-collisional regime. As noted earlier, the magnetic Prandtl number is $P_m = 0.1$. In our nonlinear computations, the S-value is either 5×10^3 or 8×10^4. Varying d_i in the nonlinear computations allows us to study single-helicity tearing and subsequent magnetic island evolution in the single-fluid and two-fluid regimes. To examine the effect of warm ions, i.e., ion gyroviscosity, we run each case twice: once with warm ions ($f_{Ti} = 0.5$) and once with cold ions ($f_{Ti} = 0$).

IV. LINEAR TEARING ANALYSIS

A. Linear growth rates

Figure 2 shows linear growth rates vs ρ_s for calculations with cold ($f_{Ti} = 0$) and warm ions ($f_{Ti} = 0.5$) at $S = 8 \times 10^4$. From analytical theory for tearing in slab geometry, we expect electron–ion decoupling to be important when ρ_s exceeds the resistive skin depth.[15,16] Using the single-fluid growth rate to compute the skin depth, we have $\delta = 0.067a$ and the cold-ion trace shows growth rates that depart from the MHD result by about 20% at $\rho_s = \delta$. Thus, our cylindrical results with cold ions are consistent with

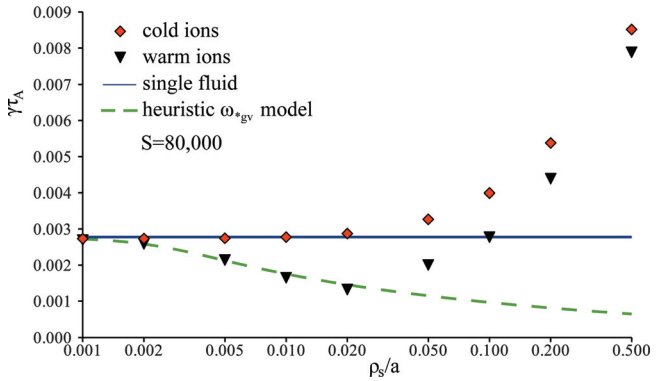

FIG. 2. (Color online) Growth rates ($\gamma\tau_A$) vs the ion sound gyroradius (ρ_s) for linear computations with cold ions ($f_{Ti}=0$, diamonds) and warm ions ($f_{Ti}=0.5$, triangles). The single-fluid result is shown as the solid horizontal line, and heuristic ω_{*gv}-model growth rate is the dashed line. These ρ_s scans are performed at $S=8\times10^4$ and $\beta=0.1$.

expectations from the analytical theory. Our results with warm ions show a more complicated transition. In the small-ρ_s limit, both the warm- and cold-ion results approach the single-fluid growth rate. At large-ρ_s values, the electron flow decouples from the ion flow such that the warm-ion effects are not important. Thus, the warm- and cold-ion growth rates also converge at large ρ_s. In the intermediate regime, the ion response is modified by a drift effect from the ion gyroviscosity. This drift effect leads to growth rates that are smaller than the single-fluid result when ρ_s is not large enough for the KAW response to decouple the tearing from the ion fluid. Numerical results for similar warm-ion conditions in slab geometry do not show this drift regime, so the important gyroviscous effect is associated with the cylindrical geometry and equilibrium.

We examine the gyroviscous effects in our pinch profiles by considering the parallel component of the vorticity equation,

$$\hat{\mathbf{b}}\cdot\nabla\times\left(\rho\frac{d\mathbf{v}}{dt}+\nabla\cdot\mathbf{\Pi}\right)=\hat{\mathbf{b}}\cdot\nabla\times(\mathbf{J}\times\mathbf{B}). \tag{6}$$

As discussed in Chapter 7 of Ref. 32, a stress tensor makes two contributions. The first appears directly on the left-hand side of Eq. (6), and the second appears when eliminating $\nabla_\perp B$ after writing the Lorentz force on the RHS in terms of the curvature vector $\boldsymbol{\kappa}$. With uniform background mass density and dropping the small inward pinch flow, the linear version of this vorticity equation for $\exp(-i\omega t)$ time dependence is

$$\begin{aligned}-i\omega m_i n_0\tilde{U}=&-m_i n_0\mathbf{v}_0\cdot\nabla\tilde{U}+B_0(\mathbf{B}_0\cdot\nabla)\frac{\tilde{J}_\parallel}{B_0}\\&+B_0(\tilde{\mathbf{B}}\cdot\nabla)\frac{J_{\parallel0}}{B_0}+2\hat{\mathbf{b}}_0\times\boldsymbol{\kappa}_0\cdot\left(\nabla\tilde{p}+\nabla\cdot\tilde{\Pi}\right)\\&-\hat{\mathbf{b}}_0\cdot\nabla\times\nabla\cdot\tilde{\Pi},\end{aligned} \tag{7}$$

where $\boldsymbol{\kappa}_0\equiv\hat{\mathbf{b}}_0\cdot\nabla\hat{\mathbf{b}}_0=-\hat{r}b_\theta^2/r$, $b_\theta=B_{\theta0}/B_0$, and the parallel vorticity is $\tilde{U}=\hat{\mathbf{b}}_0\cdot\nabla\times\tilde{\mathbf{v}}$. The tilde here indicates perturbed fields. We assemble a heuristic dispersion relation using resistive-MHD magnetic-field evolution and just the component of the flow that is associated with tearing vortices, $\tilde{\mathbf{v}}=\hat{\mathbf{b}}_0\times\nabla\tilde{\phi}$ with a streamfunction $\tilde{\phi}$. A complete dispersion relation would include both the finite-β effects that couple parallel flows and the two-fluid Ohm's law. However, through comparison with the results from NIMROD, we show that our heuristic model explains the stabilizing gyroviscous effect in the drift regime at intermediate-ρ_s values.

The gyroviscous effects on the tearing vortices are most significant near the resonant surface, r_s, where $q(r_s)=m/n$ for helical perturbations that vary in θ and z as $\exp(im\theta-inz/R)$. We therefore expand the gyroviscous stress operator about r_s. Variation of the direction and magnitude of the equilibrium magnetic field are important for pinch profiles, so they are expanded about the resonant surface: $\hat{\mathbf{b}}_0=\hat{\mathbf{b}}_0(r_s)+x\hat{\mathbf{b}}_0'+(1/2)x^2\hat{\mathbf{b}}_0''+\cdots$, for example, where $x\equiv r-r_s$ and we consider $|x|\sim\epsilon r_s$ with $\epsilon\ll1$. The wavenumber vector, $\mathbf{k}=\hat{\theta}m/r-\hat{z}n/R$, is similarly expanded about r_s. For these equilibrium and geometric quantities, primes indicate differentiation with respect to r, evaluated at $r=r_s$. For the perturbed streamfunction, $\tilde{\phi}(x)$, primes indicate derivatives with respect to x. The localized nature of the tearing response leads to an ordering with respect to x with each derivative of $\tilde{\phi}$ lowering the order of a term by ϵ. Unlike a flute ordering, the wavenumber of the tearing mode, $k_\perp=\sqrt{(m/r)^2+(n/R)^2}$, is order 1. Thus the leading-order radial flows $\tilde{v}_r=-ik_\perp\tilde{\phi}$ are order ϵ smaller than the leading-order perpendicular flows, $\tilde{v}_\perp=\tilde{\phi}'$, where perpendicular ($\perp$) and parallel ($\|$) refer to the magnetic coordinates ($\hat{\mathbf{r}}$, $\hat{\mathbf{e}}_\perp=\hat{\mathbf{b}}_0\times\hat{\mathbf{r}}$, $\hat{\mathbf{e}}_\|=\hat{\mathbf{b}}_0$) at $r=r_s$. Higher-order contributions result from the expansions of $\hat{\mathbf{b}}_0$ and $\mathbf{k}$.

While forces from the gyroviscous stress of the tearing vortices include terms as large as order ϵ^{-3}, many do not contribute to the parallel vorticity. The leading-order force, $(p_{i0}\tilde{\phi}'''/2\omega_{ci0})\hat{\mathbf{r}}$, for example, does not have a component in the $\hat{\mathbf{b}}_0\times\boldsymbol{\kappa}_0$ direction. Including terms of order ϵ^{-2}, the force is

$$\begin{aligned}-\nabla\cdot\tilde{\mathbf{\Pi}}=&\left[\frac{p_{i0}}{2\omega_{ci0}}\left(\tilde{\phi}'''+\frac{\tilde{\phi}''}{r}\right)+\left(\frac{p_{i0}}{2\omega_{ci0}}\right)'\left(\tilde{\phi}''+x\tilde{\phi}'''\right)\right]\hat{\mathbf{r}}\\&+\frac{p_{i0}}{2\omega_{ci0}}ik_\perp\tilde{\phi}''\hat{\mathbf{b}}_0\times\hat{\mathbf{r}}+\mathcal{O}(\epsilon^{-1}).\end{aligned} \tag{8}$$

From this, we find the leading-order curvature induced modification to $\hat{\mathbf{b}}_0\cdot\nabla\times(\mathbf{J}\times\mathbf{B})$,

$$2\hat{\mathbf{b}}_0\times\boldsymbol{\kappa}_0\cdot\nabla\cdot\tilde{\mathbf{\Pi}}=\frac{p_{i0}}{\omega_{ci0}}\frac{b_\theta^2}{r}ik_\perp\tilde{\phi}''+\mathcal{O}(\epsilon^{-1}). \tag{9}$$

The leading-order forces in the radial and perpendicular directions, of order ϵ^{-3} and ϵ^{-2}, respectively, in Eq. (8), may be viewed as

$$-\nabla\cdot\tilde{\mathbf{\Pi}}\cong\frac{p_{i0}}{2\omega_{ci0}}\left[\left(\nabla^2\tilde{v}_\perp\right)\hat{\mathbf{r}}-\left(\nabla^2\tilde{v}_r\right)\hat{\mathbf{b}}_0\times\hat{\mathbf{r}}\right]. \tag{10}$$

Figure 3 shows that when the expression on the RHS is computed with the flow velocity of the warm-ion tearing mode, it provides a good approximation to the full gyroviscous force.

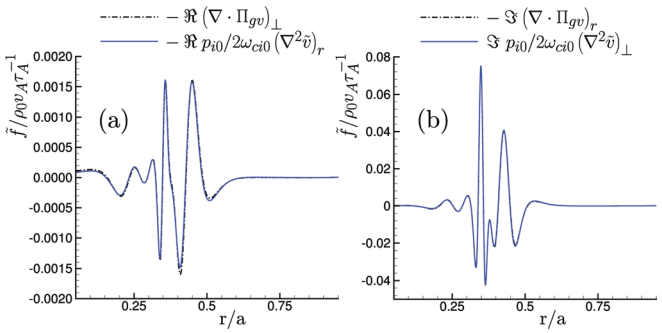

FIG. 3. (Color online) The perpendicular, (a), and radial, (b), ion-gyroviscous stress as well as the leading-order terms expressed in Eq. (10) for a linear computation with $S = 8 \times 10^4$, $\beta = 0.1$, $\rho_s = 0.05a$, and warm ions.

The order ϵ^{-3} terms proportional to $\tilde{\phi}_1''' \simeq \nabla^2 \tilde{v}_\perp$ cancel in $-\hat{\mathbf{b}}_0 \cdot \nabla \times \nabla \cdot \tilde{\mathbf{\Pi}}$, where this cancellation is related to the nearly incompressible nature of the tearing flows, i.e., the lowest-order terms become $-(p_{i0}/2\omega_{ci0})\nabla^2(\nabla \cdot \tilde{\mathbf{v}})$. Thus, to calculate the parallel gyroviscous torque to order ϵ^{-2}, we calculate the force to order ϵ^{-1}. After this calculation, detailed in the Appendix, we find

$$-\hat{\mathbf{b}}_0 \cdot \nabla \times \nabla \cdot \tilde{\mathbf{\Pi}} = \frac{p_{i0}}{2\omega_{ci0}} \frac{b_\theta^2}{r} ik_\perp \tilde{\phi}'' + \left(\frac{p_{i0}}{\omega_{ci0}}\right)' ik_\perp \tilde{\phi}'' + \mathcal{O}(\epsilon^{-1}), \tag{11}$$

which is of the same order as the leading contribution from $2\hat{\mathbf{b}}_0 \times \boldsymbol{\kappa}_0 \cdot \nabla \cdot \tilde{\mathbf{\Pi}}$. Using $\tilde{U} \simeq \tilde{\phi}''$ to order ϵ^{-2} and ignoring contributions from the relatively small isotropic viscosity, we rewrite the parallel-vorticity equation as

$$-m_i n_0 i(\omega + \omega_{*gv})\tilde{U} = B_0 \mathbf{B}_0 \cdot \nabla \left(\frac{\tilde{J}_\parallel}{B_0}\right) + \frac{B_0}{a\mu_0}\left(\tilde{\mathbf{B}} \cdot \nabla\right)\lambda_0 + 2\hat{\mathbf{b}}_0 \times \boldsymbol{\kappa}_0 \cdot \nabla \tilde{p}, \tag{12}$$

where

$$\omega_{*gv} = \frac{k_\perp}{m_i n_0} \frac{p_{i0}}{\omega_{ci0}} \left(\frac{3}{2}\frac{b_\theta^2}{r} - \frac{B_0'}{B_0}\right) = k_\perp f_{Ti} \beta d_i v_A \left(\frac{3}{2}\frac{b_\theta^2}{r} - \frac{B_0'}{B_0}\right). \tag{13}$$

For conditions with an ion diamagnetic drift, $\mathbf{v}_0 = \hat{\mathbf{b}}_0 \times \nabla p_{i0}/\omega_{ci0} m_i n_0$, the advective term of Eq. (7) becomes $-ik_\perp p_{i0}' \tilde{U}/\omega_{ci0}$ and cancels with the contribution from the ion-gyroviscous torque that is proportional to p_{i0}' in Eq. (11). Thus, even though we study cases without an equilibrium-pressure gradient, we recover the general lowest-order effects with respect to ρ_i/L in the ion-flow equation.

The ω_{*gv} term from gyroviscous stress has the form of an ion-drift effect in the parallel vorticity equation, and it provides stabilizing effects that are generally observed with drift-tearing.[11] To demonstrate the stabilizing effects, we ignore terms from the perturbed pressure and equilibrium flow in the parallel-vorticity equation, Eq. (12), and combine it with resistive-MHD evolution of the perturbed magnetic flux, $\tilde{\psi}$, using $\tilde{\mathbf{B}} = \nabla\tilde{\psi} \times \mathbf{B}_0 + \tilde{B}_\parallel \hat{b}$ where each derivative

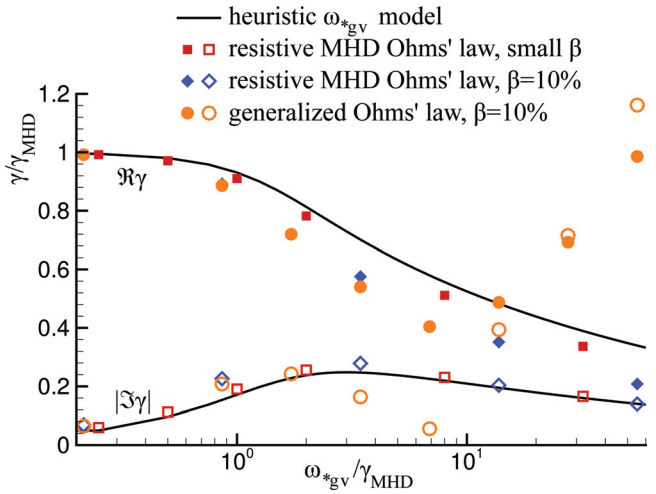

FIG. 4. (Color online) A comparison of $\Re\gamma$ (top curve, filled symbols) and $|\Im\gamma|$ (bottom curve, open symbols) between the heuristic ω_{*gv} model and three sets of numerical computations with $S = 10^6$, $P_m = 10^{-3}$, and ion gyroviscosity.

with respect to $x \sim \epsilon r_s$ of $\tilde{\psi}(x)$ is ordered as ϵ^{-1}. This results in a coupled pair of second-order differential equations,

$$\left(\gamma - i\omega_{*gv}\right)\tilde{U} = -v_A^2 ik_\parallel' x\tilde{\psi}'', \qquad \gamma\tilde{\psi} + ik_\parallel' x\tilde{\phi} = \frac{\eta}{\mu_0}\tilde{\psi}'', \tag{14}$$

where $\gamma = -i\omega$ and $\tilde{J}_\parallel \cong -(B_0/\mu_0)\,\tilde{\psi}''$ to leading order as in Ref. 32, for example. Using these as our inner-layer equations for the tearing mode, the resulting heuristic dispersion relation is $\gamma^4(\gamma - i\omega_{*gv}) = \gamma_{MHD}^5$, where γ_{MHD} is the growth rate in the MHD limit.

In Fig. 4, we compare the growth rate and real frequency of the heuristic dispersion relation with results from three sets of linear computations from NIMROD with $S = 10^6$ and $P_m = 10^{-3}$. The first set uses a resistive-MHD Ohm's law with the cylindrical geometry and parameters of our pinch case, and β is very small in order to reproduce the simplified response assumed for the heuristic model. Thus to capture the effects of ion gyroviscosity, an *ad hoc* gyroviscous coefficient is scaled to vary ω_{*gv}. Although the numerical computations include more than just the leading-order effects with respect to $|x|/a$, we see that there is good agreement between our heuristic model and the growth rate and real frequency computed with NIMROD, and a strong stabilizing effect from the gyroviscous stress is apparent. The second set of numerical computations shown in the figure are computed with $\beta = 10\%$ and $f_{Ti} = 0.5$; the Ohm's law is again resistive MHD. Although the heuristic model does not include coupling between parallel flow and perturbed pressure, we observe that there is semi-quantitative agreement with the heuristic model underpredicting the stabilizing effect at large-ω_{*gv} values. The third set of computations uses the generalized Ohm's law, Eq. (1), and essentially the same parameters as the computations shown in Fig. 2 except that $S = 10^6$ and $P_m = 10^{-3}$. The results are similar to those with $\beta = 10\%$ and the resistive-MHD Ohm's law up to $\omega_{*gv}/\gamma_{MHD} \simeq 10$ where the real frequency changes sign as the KAW-type effects become important. Note that ω_{*gv} is

proportional to the ion-sound gyroradius and in our computations, $\omega_{*gv}/\gamma_{MHD} \simeq 1100\rho_s/a$. Thus, the gyroviscous contribution becomes important at $\rho_s/a \simeq 1 \times 10^{-3}$, before KAW responses occur, and loses significance for $\rho_s/a \gtrsim \delta/a \simeq 2 \times 10^{-2}$.

These scalings are consistent with the results for warm ions shown in Fig. 2, where the growth rate from the heuristic model is also shown. For $S = 8 \times 10^4$, $\omega_{*gv} \simeq \gamma_{MHD}$ at $\rho_s/a = 0.002$, and we conclude that a single-fluid MHD model captures the physics when $\omega_{*gv} < \gamma_{MHD}$, the drift regime begins when $\omega_{*gv} \gtrsim \gamma_{MHD}$, and KAW decoupling effects dominate when $\rho_s \gtrsim \delta$.

B. Linear tearing mode structure

When examining the phase relations and flow patterns of the two-fluid tearing mode in cylindrical geometry, it is useful to start by comparing them with tearing in a more idealized slab geometry with two highly conducting walls at $x = \pm a$. In standard slab analysis, the force-free equilibrium current, $\mathbf{J}_0 = \lambda(x)\,\mathbf{B}_0/\mu_0 a$, is in the yz-plane, and the function $\lambda(x)$ is assumed to be symmetric with respect to $x = 0$, where the resonant condition, $\mathbf{k}\cdot\mathbf{B}_0 = 0$, is satisfied. The equilibrium magnetic field has no curvature, and with uniform pressure, its magnitude is also uniform. The electron flows of tearing modes in this simple configuration symmetrically advect the reconnecting magnetic flux into a magnetic island, as illustrated schematically in Fig. 5. Because these vortices are required for reconnection, similar flows occur in cylindrical geometry. However, field-line curvature, an asymmetric parallel-current profile with respect to the position of the resonant surface, and mathematical regularity conditions at $r = 0$ affect the eigenfunction. We choose the phase such that $\tilde{B}_r(0)$ is positive and real, as shown in the schematic. With a single-fluid resistive MHD model, this choice makes $\tilde{B}_r(r)$ purely real and $\tilde{B}_\perp(r)$ and $\tilde{B}_\parallel(r)$ purely imaginary.[33] The x-point inflow is then part of the purely imaginary $\tilde{v}_r(r)$, and the x-point outflow is part of the purely real $\tilde{v}_\perp(r)$.

Two-fluid effects alter the phases of the tearing eigenfunction as a function of radius, so the single-fluid phase relations are not valid. In Figs. 6 and 7, we plot two different sets of computed eigenfunction components for different physical parameters. The first set corresponds to the nonzero perturbations in the single-fluid limit ($\Re\tilde{B}_r$, $\Im\tilde{B}_\perp$, $\Im\tilde{B}_\parallel$), and the second set ($\Im\tilde{B}_r$, $\Re\tilde{B}_\perp$, $\Re\tilde{B}_\parallel$) is nonzero only when two-fluid effects are considered. The linear magnetic components

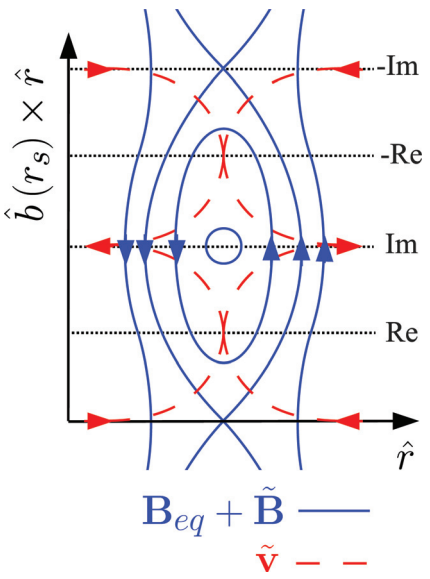

FIG. 5. (Color online) A schematic of a slab tearing mode. The solid lines illustrate the magnetic topology of the mode, and the dashed lines show the flows that transport the reconnecting magnetic flux. Real and imaginary parts of the Fourier coefficients are equivalent to radial slices of the schematic as indicated.

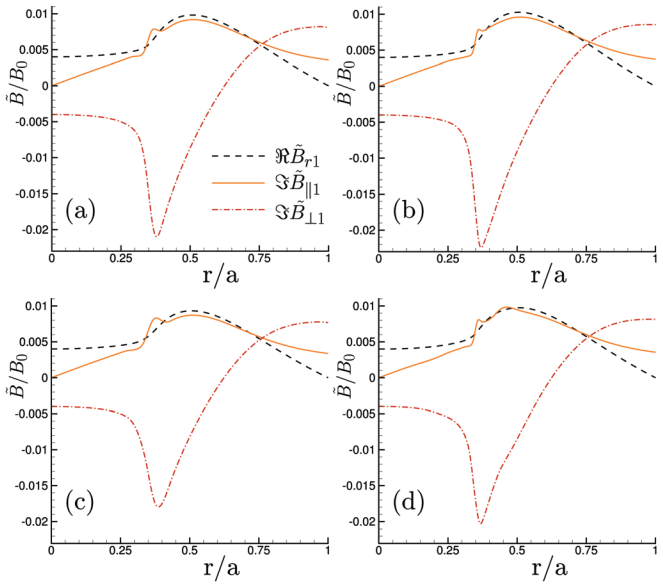

FIG. 6. (Color online) Eigenmode components of $\tilde{\mathbf{B}}$ in phase with a single-fluid eigenfunction for computations with $S = 8 \times 10^4$, $\beta = 0.1$ and (a) $\rho_s = 0.01a$ and cold ions, (b) $\rho_s = 0.05a$ and cold ions, (c) $\rho_s = 0.01a$ and warm ions, and (d) $\rho_s = 0.05a$ and warm ions.

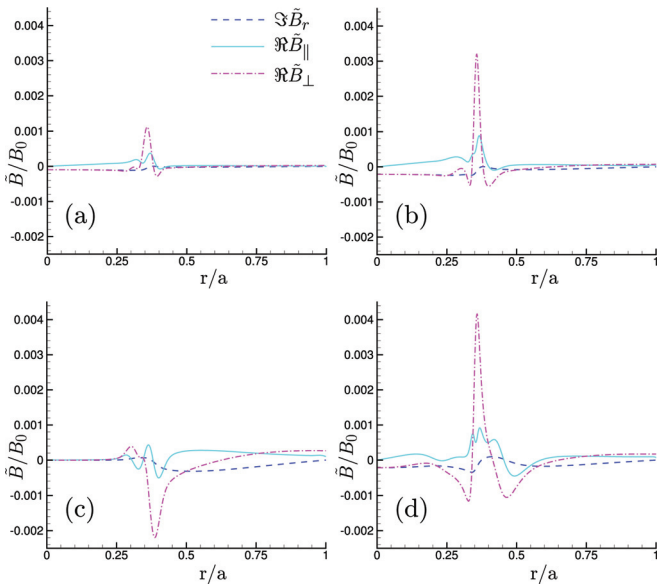

FIG. 7. (Color online) Eigenmode components of $\tilde{\mathbf{B}}$ out of phase with a single-fluid eigenfunction for computations with $S = 8 \times 10^4$, $\beta = 0.1$ and (a) $\rho_s = 0.01a$ and cold ions, (b) $\rho_s = 0.05a$ and cold ions, (c) $\rho_s = 0.01a$ and warm ions, and (d) $\rho_s = 0.05a$ and warm ions.

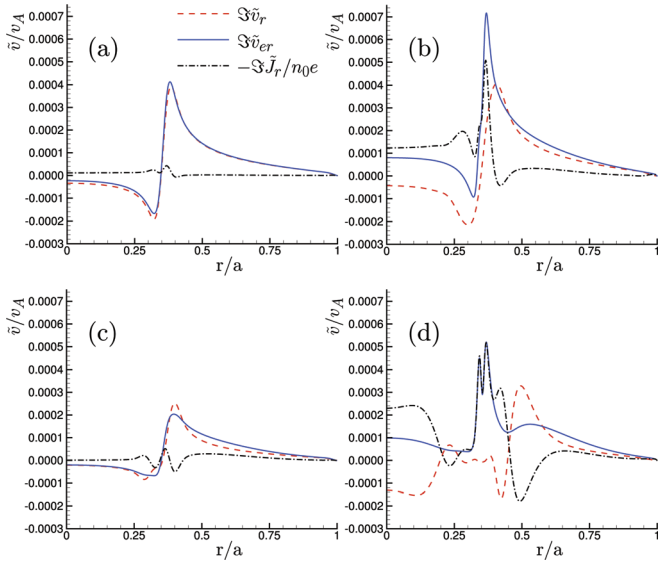

FIG. 8. (Color online) Linear electron and ion reconnecting flows and the difference, $\tilde{\mathbf{J}}/ne$. The radial components (x-point inflow) are displayed for computations with $S = 8 \times 10^4$, $\beta = 0.1$ and (a) $\rho_s = 0.01a$ and cold ions, (b) $\rho_s = 0.05a$ and cold ions, (c) $\rho_s = 0.01a$ and warm ions, and (d) $\rho_s = 0.05a$ and warm ions.

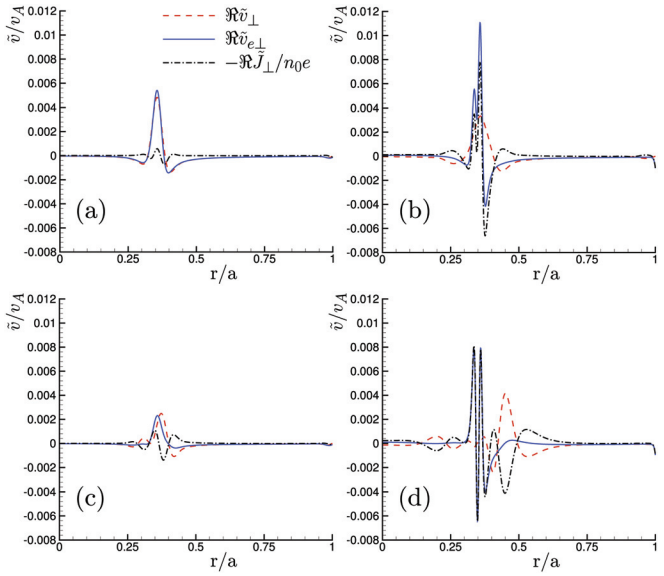

FIG. 9. (Color online) Linear electron and ion reconnecting flows and the difference, $\tilde{\mathbf{J}}/ne$. The perpendicular components (x-point outflow) are shown for computations with $S = 8 \times 10^4$, $\beta = 0.1$ and (a) $\rho_s = 0.01a$ and cold ions, (b) $\rho_s = 0.05a$ and cold ions, (c) $\rho_s = 0.01a$ and warm ions, and (d) $\rho_s = 0.05a$ and warm ions.

of the first set at $S = 8 \times 10^4$ are plotted in Fig. 6 for $\rho_s = 0.01a$ and $\rho_s = 0.05a$ with warm and cold ions. The amplitude of the eigenfunction has been normalized such that $\Re\tilde{B}_r(0) = 0.004B_0$ for comparison with the nonlinear plots discussed in Sec. V. Note that the profile and relative amplitude of the ($\Re\tilde{B}_r$, $\Im\tilde{B}_\perp$, $\Im\tilde{B}_\parallel$) components are largely unchanged by the two-fluid effects. A straightforward application of Ampere's law shows that the magnetic perturbations ($\Re\tilde{B}_r$, $\Im\tilde{B}_\perp$, $\Im\tilde{B}_\parallel$) produce a current perturbation with the phase orientation ($\Re\tilde{J}_r$, $\Im\tilde{J}_\perp$, $\Im\tilde{J}_\parallel$). The two-fluid mode also has magnetic components of the second set, i.e., out of phase with the single-fluid magnetic field, that become larger as ρ_s is increased as well as with a warm-ion population. These out-of-phase components produce a current density perturbation ($\Im\tilde{J}_r$, $\Re\tilde{J}_\perp$, $\Re\tilde{J}_\parallel$) that is in phase with the flows associated with reconnection.

The out-of-phase components of $\tilde{\mathbf{J}}$ demonstrate that the electron flow required for reconnection decouples from the ion flow as ρ_s is increased. Figures 8 and 9 compare components relevant to a reconnecting electron and ion flow, as well as their separation, $\tilde{\mathbf{J}}/n_0e$. At $\rho_s = 0.05a$, the electron inflow and outflow are comparable to the relevant components of $-\tilde{\mathbf{J}}/n_0e$ near the resonant surface, and the ion flows are much smaller. This is in contrast to the smaller-ρ_s results, where the ion and electron flows are closely coupled, especially with cold ions. We note that the x-point outflow velocity is an order of magnitude larger than the inflow velocity, consistent with the ordering of Sec. IV A where $\tilde{v}_r \sim O(\epsilon^0)$ and $\tilde{v}_\perp \sim O(\epsilon^{-1})$. In the cases with cold ions, the peak of the outflow velocity is only slightly shifted from the resonant surface, indicating that the asymmetry of the cylindrical geometry has only a moderate influence. In the warm-ion $\rho_s = 0.05a$ case, the peak of $\tilde{v}_\perp$ shifts outward, and the ion flows do not penetrate all the way to the resonant surface. We surmise that the oscillations in radius are part of the drift-tearing-like behavior at finite ω_{*gv}, where the equilibrium curvature and gradient effects are important.

C. Dynamo contribution to the electric field inferred from the linear mode

With nonlinear evolution, correlated fluctuations of electron flows and magnetic field can modify the mean field via the generation of a dynamo emf. The dominant contributions to the average electric field are

$$\langle \mathbf{E} \rangle \equiv \mathbf{E}_0 \cong -\mathbf{v}_0 \times \mathbf{B}_0 + \eta \mathbf{J}_0 - \langle \tilde{\mathbf{v}} \times \tilde{\mathbf{B}} \rangle + \left\langle \frac{\tilde{\mathbf{J}} \times \tilde{\mathbf{B}}}{n_0 e} \right\rangle, \quad (15)$$

where $\langle x \rangle = (1/4\pi^2 R) \int x d\theta dz$ indicates an average over the poloidal and axial directions. Together, the last two terms on the RHS of Eq. (15) are the fluctuation-induced dynamo emf, $\mathbf{E}_f$. The first of these terms represents the MHD-dynamo effect, while the second is the Hall-dynamo effect.

Figure 10 shows the parallel component of the dynamo emfs calculated from the linear eigenfunctions, where parallel is with respect to the equilibrium magnetic field. In the cold-ion small-ρ_s regime, case (a), where ion and electron flows are coupled, the Hall dynamo is small and the MHD dynamo dominates. Since the MHD and Hall dynamo are flux-surface averages, the results follow from the relationship between the phases of the fluctuation components that determine the cross product in the quadratic dynamo terms. In the single-fluid limit, the perpendicular component of reconnecting ion flow, $\tilde{v}_\perp(r)$, and the radial component of the magnetic perturbation, $\tilde{B}_r(r)$, as well as the pair of the functions $\tilde{v}_r(r)$ and $\tilde{B}_\perp(r)$, are in phase and contribute to the axisymmetric MHD-dynamo electric field. However, as discussed in Sec. IV B, in the single-fluid limit the perpendicular and radial components of the current perturbation are out

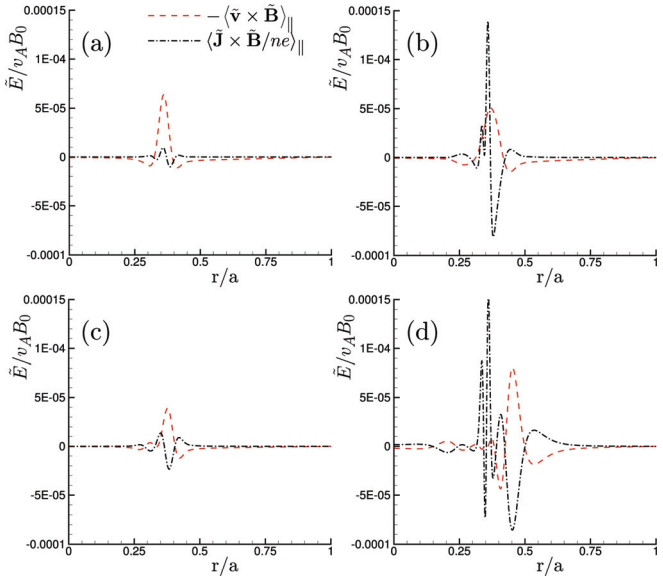

FIG. 10. (Color online) The dynamo electric fields inferred from the linear eigenmodes for computations with $S = 8 \times 10^4$, $\beta = 0.1$ and (a) $\rho_s = 0.01a$ and cold ions, (b) $\rho_s = 0.05a$ and cold ions, (c) $\rho_s = 0.01a$ and warm ions, and (d) $\rho_s = 0.05a$ and warm ions.

of phase with respect to the corresponding magnetic components; thus, the quasilinear Hall dynamo vanishes. In contrast, the Hall contribution is significant in the two-fluid regimes (b and d) where the electron and ion fluids decouple and a fraction of the perturbed current arises in phase with the corresponding magnetic components. This effect is described in more detail for slab geometry in Ref. 6.

With cold ions and $\rho_s = 0.05a$, Fig. 10(b), the Hall dynamo peaks near the rational surface and adds to the MHD dynamo. Away from the rational surface, they tend to cancel. The peaked structure of the Hall dynamo near the rational surface qualitatively agrees with the analytic prediction at large ρ_s in Ref. 6. However, the dynamo is an even function about the resonant surface in slab geometry with a symmetric λ profile, whereas it is an odd function in our cylindrical cases. The inclusion of warm ions and ion gyroviscosity results in further decoupling of the ion and electron fluids and appreciable Hall dynamo even at small ρ_s, as shown in Fig. 10(c). With warm ions and $\rho_s = 0.05a$, case (d), the Hall dynamo is more significant, and strongly peaked at the resonant surface with fine structure. Figures 8(d) and 9(d) demonstrate that the ions do not penetrate to the resonant surface, and an eddy forms on the outboard side. Figure 10(d) shows that the resulting MHD dynamo also shifts outward, but it is largely canceled by the Hall dynamo.

V. NONLINEAR SATURATION

We now consider results from fully nonlinear computations, where the perturbations modify the mean field via the dynamo emf and the mode saturates. We run the computations through the Rutherford stage,[20] where the nonlinear profile modification affects the growth of the mode, to a nearly steady final state. Figure 11 plots the island width in time for cold and warm ions at $S = 8 \times 10^4$ with $\rho_s = 0.05a$. Early in the nonlinear evolution, the island-width evolution

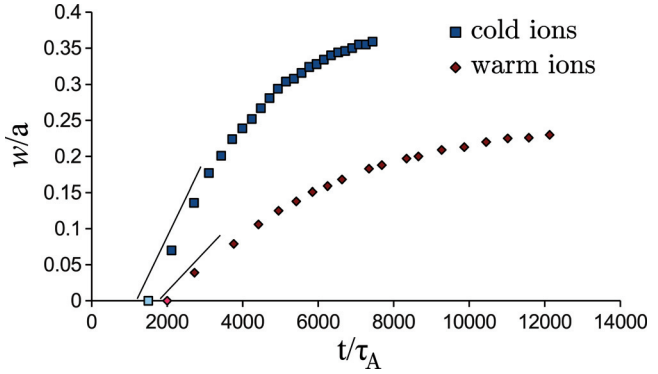

FIG. 11. (Color online) The island width as a function of time for computations with warm- and cold-ion models and $\rho_s = 0.05a$, $S = 8 \times 10^4$, and $\beta = 0.1$. The lighter colored data points at $w(t) = 0$ represent the earliest indications of nonlinear evolution.

is characteristic of the Rutherford stage with nearly linear growth: $dw/dt = A\Delta'\eta/\mu_0$ where w is the island width and A is a coefficient of order unity. Spectral broadening to $m \geq 2$ is allowed in the simulations, but it is not observed to be significant.

A. Saturated island structure

As discussed in Sec. IV B, the linear MHD eigenfunction can be normalized such that $\Im\tilde{B}_r(r) = \Re\tilde{B}_\perp(r) = \Re\tilde{B}_\parallel(r) = 0$. This relation among the phases of the components is approximately valid for the nonlinear saturated structures. The dominant part of the magnetic-field perturbation, for the $\rho_s = 0.05a$ cases at $S = 8 \times 10^4$, is $\Re\tilde{B}_r(r)$, $\Im\tilde{B}_\perp(r)$, and $\Im\tilde{B}_\parallel(r)$ which are in phase with the single-fluid eigenfunction (see Fig. 12). Including the effect of ion gyroviscosity from warm ions reduces the saturation amplitude in the $\rho_s = 0.05a$ cases, although the shape of the perturbations is largely unchanged. This result is not sensitive to the Lundquist number, at least in the conditions tested numerically between $S = 5000$ and 8×10^4. For both the warm- and cold-ion cases, the shape of the perturbations is reminiscent of the linear results in Fig. 6 with the sharper features washed out. A notable difference is the large peak of $\Im\tilde{B}_\perp$ that is only present in the linear results. This can be qualitatively explained through use of the $\nabla \cdot \mathbf{B} = 0$ constraint. One expects that $\Im\tilde{B}_\perp$ scales like $\Re\tilde{B}_r/kw$ in the nonlinear stage, whereas it scales like $\Re\tilde{B}_r/k\delta$ in the linear stage. Thus,

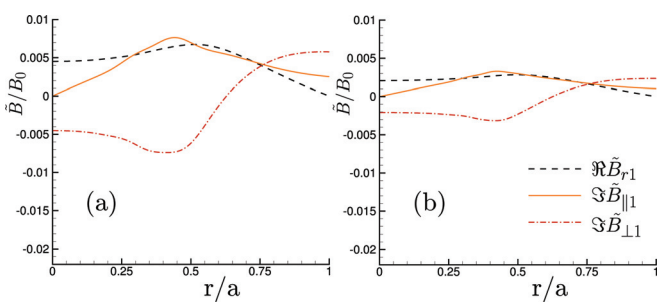

FIG. 12. (Color online) Components of $\tilde{\mathbf{B}}$ from a saturated island in phase with a single-fluid eigenfunction for computations with $S = 8 \times 10^4$, $\beta = 0.1$, $\rho_s = 0.05a$ and (a) cold ions and (b) warm ions.

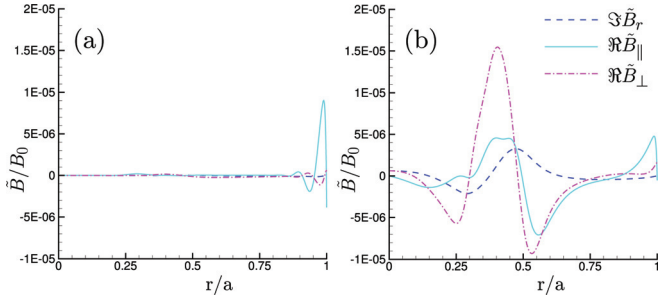

FIG. 13. (Color online) Components of $\tilde{\mathbf{B}}$ from a saturated island out of phase with a single-fluid eigenfunction for computations with $S = 8 \times 10^4$, $\beta = 0.1$, $\rho_s = 0.05a$ and (a) cold ions and (b) warm ions.

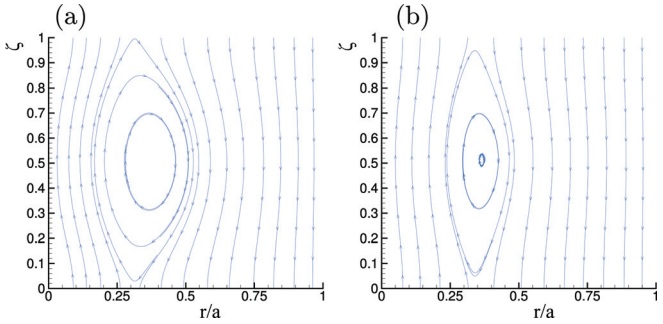

FIG. 14. (Color online) Streamlines of a helical projection of $\mathbf{B}_{eq} + \tilde{\mathbf{B}}$ for computations with $S = 8 \times 10^4$, $\beta = 0.1$, $\rho_s = 0.05a$ and (a) cold ions and (b) warm ions.

relative to $\Re\tilde{B}_r$, the peak of $\Im\tilde{B}_\perp$ is expected to be $\sim \delta/w$ smaller in the nonlinear stage.

The saturated magnetic perturbations which are out of phase with the single-fluid eigenfunction are plotted in Fig. 13. The amplitude of the out-of-phase components is 2 orders of magnitude smaller than the saturated in-phase magnetic components. This contrasts with the linear results (Fig. 7), where the magnitude of the out-of-phase magnetic perturbations are approximately one third of the corresponding in-phase component magnitude. In the linear cases, the large out-of-phase magnetic components are associated with induction through the relatively large, decoupled, reconnecting flows. In contrast, the flows are much smaller in the saturated state, as they only advect enough flux into the island to balance the resistive dissipation.

To help visualize the saturated states, we project the single-helicity perturbations onto a helical surface that captures the variations across the magnetic island. We make a parametric definition of a set of nested surfaces in cylindrical coordinates,

$$\left\{ r,\ \frac{2\pi m\zeta}{m^2 + (nr/R)^2} - h,\ \frac{nr^2}{R}\frac{2\pi\zeta}{m^2 + (nr/R)^2} + \frac{mR}{n}h \right\}, \quad (16)$$

where $0 \le r \le a$ is the radial coordinate, $0 \le \zeta \le 1$ is a normalized helical coordinate along a given helical surface, and $0 \le h \le (na/R)^2(2\pi/[m^2 + (na/R)^2])$ is a helical-surface label. The projection of the single-helicity perturbations onto these surfaces is independent of surface choice. A single helical surface is given by a fixed value of h and can be defined as

$$H_h(r,\ \theta,\ z) = \frac{nr}{R}\theta - \frac{m}{r}z + \left(\frac{nr}{R} + \frac{m^2R}{rn}\right)h = 0\ . \quad (17)$$

We note that variations in the $\hat{\mathbf{k}}$ direction are captured on each helical surface as $\mathbf{k}\cdot\nabla H_h = 0$, but variations in $\hat{r}$ are not captured on a single helical surface, as $\hat{r}\cdot\nabla H_h \neq 0$. The surface mapped out at constant ζ is

$$H_\zeta(r,\ \theta,\ z) = m\theta + \frac{n}{R}z - 2\pi\zeta = 0\ . \quad (18)$$

As $\hat{r}\cdot\nabla H_\zeta = 0$, we conclude that variations in $\hat{r}$ merely move between the surfaces at constant ζ. Since all the H_h surfaces are identical, we choose one ($h = 0$) and project the $\hat{r}$ and $\hat{k}/L(r)$ vector components, where $L(r)$ is the helix length at a given radius, onto this surface.

It is illustrative to consider the trivial case of the helical surfaces for an $m = 0$ mode. The constant-h surfaces then become the rz planes with $\theta = -h$, and for this particular case $\hat{\mathbf{r}}\cdot\nabla H_h = 0$. The constant-$\zeta$ surfaces are the $r\theta$ planes with $z = 2\pi R\zeta/n$. Note that $0 \le z \le 2\pi R/n$, thus only one x-point and one o-point are captured on the surface for any n.

Returning to our $m = 1$ nonlinear results, Fig. 14 shows the helical projection for the full magnetic-field streamlines. To verify our helical-projection method, the width measured from these plots has been compared to the results of a puncture plot produced with magnetic-field-line tracing. As one would expect from the smaller magnetic perturbation in Fig. 12(b), the $\rho_s = 0.05a$ case with warm ions exhibits a smaller island saturation width than the cold-ion case. Table I lists the saturated island width for a larger parameter scan at $S = 5000$, as well as the two cases at $S = 8 \times 10^4$. The scan shows that for the warm-ion, $\rho_s = 0.01a$ case and all the cold-ion cases, the island width is determined by physics included in the single-fluid model. However, the island width decreases as ρ_s is increased in the warm-ion cases.

Steady single-helicity conditions require a helical electrostatic-field configuration arising from the reconnecting flows[34,35] as well as helical force balance. Our results show that the Hall term in Ohm's law does not significantly modify this electrostatic configuration when ions are cold. Thus, the final magnetic field perturbation amplitude is not affected by ρ_s. However, as discussed in Sec. V C, gyroviscous effects from warm ions modify the island force balance and thus the saturated width.

After nonlinear saturation, advection of magnetic flux into the island continues to balance resistive diffusion. This flow, plotted in Figs. 15 and 16, is analogous to the

TABLE I. Magnetic-island widths at saturation as a function of ρ_s for cases with cold and warm ions at $\beta = 0.1$.

ρ_s/a	S	w/a (cold)	w/a (warm)
Single fluid	5000	0.36	
0.01	5000	0.36	0.36
0.05	5000	0.36	0.24
0.05	8×10^4	0.36	0.24
0.20	5000	0.36	0.21

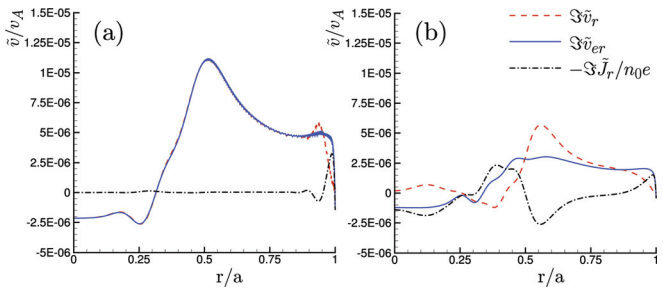

FIG. 15. (Color online) Electron and ion reconnecting flows and the difference, $\tilde{\mathbf{J}}/ne$. The radial components (x-point inflow) are displayed for computations with $S = 8 \times 10^4$, $\beta = 0.1$, $\rho_s = 0.05a$ and (a) cold ions and (b) warm ions.

equilibrium pinch flow in establishing an Ohmic steady state. Comparing the figures, we note that the general shape of the electron flows is relatively unchanged by the warm-ion effects; however, their amplitude is reduced. The eddies are larger in the cold-ion case to sustain the larger island against dissipation. The narrow structure of the linear flows is replaced by a radially broad eddy in the saturated state. The flows in the saturated nonlinear cases are roughly an order of magnitude smaller than their linear counterparts, after scaling by the magnetic-perturbation amplitude. However, we find that the ratio of the perturbed kinetic to magnetic energy of the saturated state is only a factor of 2 less that of the linear state, due to the broad flow structure in the nonlinear state.

In Fig. 17, we project the vectors and streamlines of the ion flows onto a helical surface, along with the streamlines of the magnetic field. The contributions from the axisymmetric flows are not included. The eddies in the cold-ion case support reconnection, and as Figs. 15(a) and 16(a) show, they are coupled with the electrons. The eddies in the warm-ion case are decoupled and out of phase with a reconnecting flow. Plots of the electron-flow patterns are dominated by the contribution from the current-density perturbation that is out of phase with the flow supporting reconnection and are not shown.

B. Dynamo contribution to the electric field

The island structure in the saturated state can be directly related to the conventional picture of Fig. 5, unlike the linear

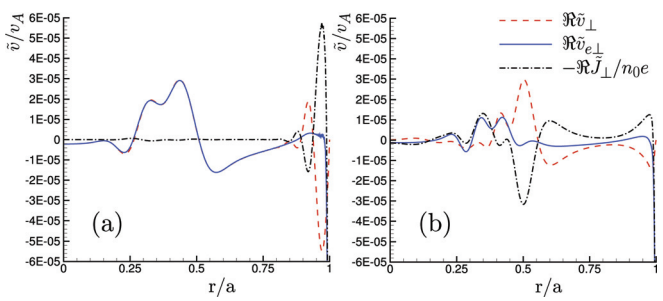

FIG. 16. (Color online) Electron and ion reconnecting flows and the difference, $\tilde{\mathbf{J}}/ne$. The perpendicular components (x-point outflow) are displayed for computations with $S = 8 \times 10^4$, $\beta = 0.1$, $\rho_s = 0.05a$ and (a) cold ions and (b) warm ions.

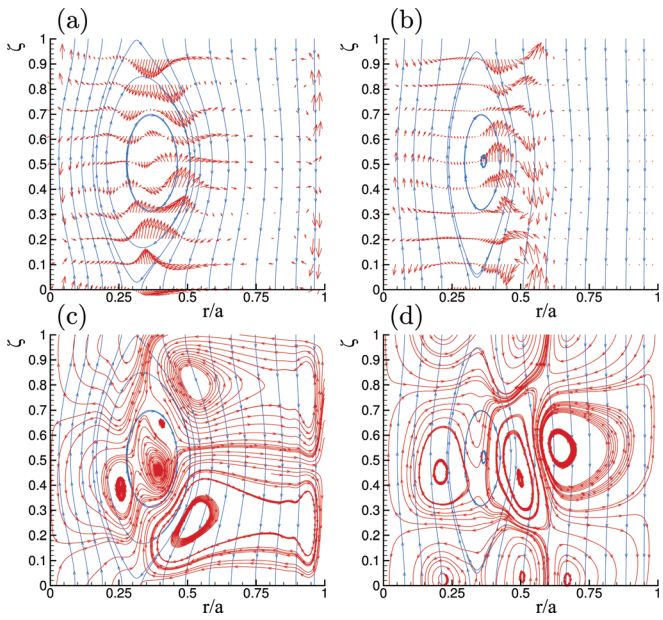

FIG. 17. (Color online) Streamlines of a helical projection of $\mathbf{B}_{eq} + \tilde{\mathbf{B}}$ for computations of a saturated island with $S = 8 \times 10^4$, $\beta = 0.1$, $\rho_s = 0.05a$. The frames also show ion flow vectors for (a) cold- and (b) warm-ion conditions, where the same vector length corresponds to a 10 × greater magnitude in the warm-ion plot. Frames (c) and (d) plot the ion-flow streamlines with cold- and warm-ion models, respectively.

cases where the perturbation is too small to affect the magnetic topology. The flow pattern of Fig. 17(c) is qualitatively similar to the flows sketched in Fig. 5 and interacts with the perturbed magnetic fields to produce the fluctuation-induced dynamo emf. It is straightforward to qualitatively determine $\mathbf{E}_f \equiv -\langle \tilde{\mathbf{v}}_e \times \tilde{\mathbf{B}} \rangle$ from Fig. 5. One expects a positive $E_{f\|}$ at the rational surface, with contributions from $\tilde{B}_r$ and $\tilde{v}_{e\perp}$ above and below the o-point. Away from the rational surface, there is a negative $E_{f\|}$ from the interaction of $\tilde{B}_\perp$ and $\tilde{v}_{er}$.

In the saturated state, the dynamo emf drives a nonlinear axisymmetric current density, $\mathscr{J}_0 \equiv \langle \mathbf{J} \rangle - \mathbf{J}_{eq}$ (the initial equilibrium field is denoted by the subscript "*eq*"), that is associated with profile changes:

$$\mathbf{E}_f = -\langle \tilde{\mathbf{v}} \times \tilde{\mathbf{B}} \rangle + \left\langle \frac{\tilde{\mathbf{J}} \times \tilde{\mathbf{B}}}{n_0 e} \right\rangle \simeq -\eta \mathscr{J}_0. \tag{19}$$

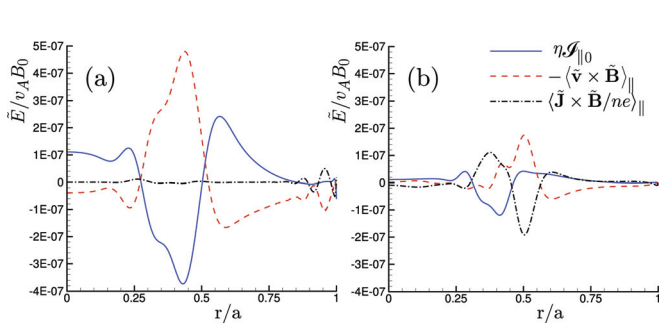

FIG. 18. (Color online) The fluctuation-induced dynamo electric fields and mean current modification at island saturation for computations with $S = 8 \times 10^4$, $\beta = 0.1$, $\rho_s = 0.05a$ and (a) cold ions and (b) warm ions.

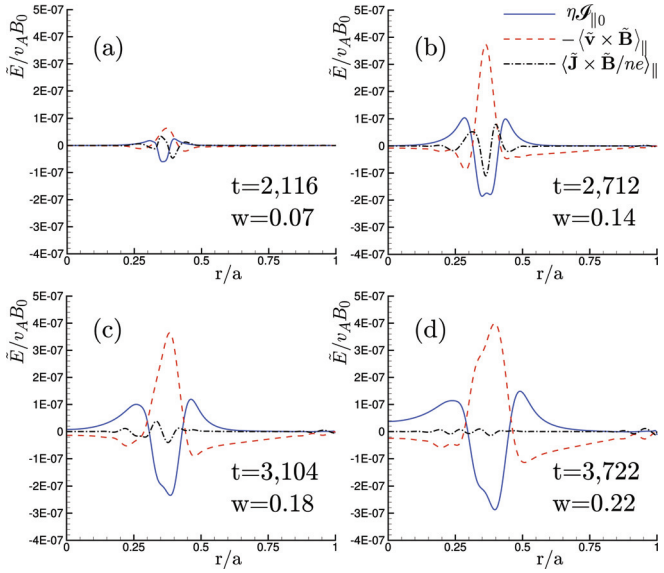

FIG. 19. (Color online) The fluctuation-induced dynamo electric fields and mean current modification for computations with $S = 8 \times 10^4$, $\beta = 0.1$, $\rho_s = 0.05a$ and cold ions at different times: (a) $t = 2116\tau_A$, (b) $t = 2712\tau_A$, (c) $t = 3431\tau_A$, and (d) $t = 3722\tau_A$.

The dynamo emfs and induced current are plotted in Fig. 18. The combined dynamo emfs produce an axisymmetric current perturbation that primarily reduces $J_{\|0}$ inside the island and increases it outside. The Hall dynamo is relevant only when the flows decouple; thus in the saturated cold-ion state with coupled flows, the MHD dynamo is dominant. In the warm-ion case, the ion flows are modified, as shown in Fig. 17(b); however, the electron flows maintain a flow pattern resembling Fig. 5, as demonstrated in Figs. 15 and 16. The Hall dynamo is significant with warm ions and the mean-current modification is smaller, which is consistent with the smaller island size.

From Figs. 10 and 18, we note that the Hall dynamo must vanish at some point in the nonlinear evolution when ions are cold. To examine this effect, Fig. 19 shows the island size and dynamo emf for the cold-ion case at different stages of nonlinear growth. The Hall dynamo becomes small relative to the MHD dynamo approximately when the island width becomes larger than $d_i = 0.17a$. In the linear cases, the two-fluid scales must be compared with the linear skin depth, δ, which is small, whereas in the nonlinear stage the two-fluid scales are compared with the island width, w, which can be considerably larger than δ.

C. Warm-ion saturation

In Rutherford theory for the resistive MHD evolution of islands, the perturbed current produces a third-order $\mathbf{J} \times \mathbf{B}$ force, where the ordering refers to the perturbation amplitude, that counteracts the linear forces driving the island growth.[20] In order to illustrate this effect, we express the $m = 1$ force-balance equation as

$$\rho_0 \frac{d\tilde{\mathbf{v}}}{dt} \cong \tilde{\mathbf{f}}_d + \tilde{\mathbf{f}}_3 - \nabla \cdot \Pi, \tag{20}$$

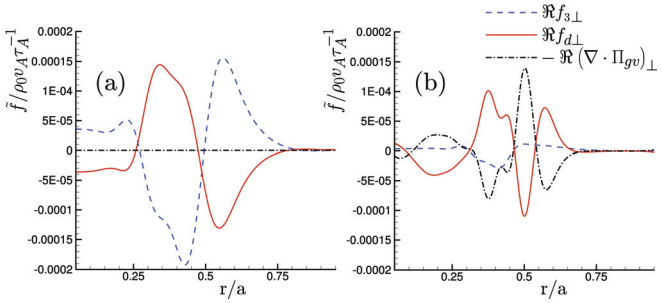

FIG. 20. (Color online) The driving, third-order and ion-gyroviscous perpendicular forces in phase with a reconnecting flow for computations with $S = 8 \times 10^5$, $\beta = 0.1$, $\rho_s = 0.05a$ and (a) cold ions and (b) warm ions.

where $\tilde{\mathbf{f}}_d$ is the driving force, and $\tilde{\mathbf{f}}_3$ is the third-order force. The driving force, $\tilde{\mathbf{f}}_d = \mathbf{J}_{eq} \times \tilde{\mathbf{B}} + \tilde{\mathbf{J}} \times \mathbf{B}_{eq} - \nabla \tilde{p}$, is the interaction of the tearing perturbation with the initial equilibrium fields. Whereas the third-order force, $\tilde{\mathbf{f}}_3 = \mathscr{J}_0 \times \tilde{\mathbf{B}}_1 + \tilde{\mathbf{J}}_1 \times \mathscr{B}_0$ with $\mathscr{B}_0 \equiv \langle \mathbf{B} \rangle - \mathbf{B}_{eq}$, is the interaction of the tearing perturbation with the profile modification from the dynamo emf. Rutherford refers to the profile modification as a second-order term as it is driven by the quadratic product of the tearing perturbations, as seen from Eq. (19).

The driving, third-order, and ion-gyroviscous perpendicular forces in phase with a reconnecting flow are plotted in Fig. 20. Contributions from the inertial and isotropic viscous terms are small. With cold ions, saturation results when the secondary force balances the driving force. However, with warm-ion effects, gyroviscosity plays a significant role in opposing the driving force, as shown in Fig. 20(b). The current profile modification required to balance $\tilde{\mathbf{f}}_d$ is smaller as $\tilde{\mathbf{f}}_3$ and $\nabla \cdot \Pi_{gv}$ combine to oppose the driving force. Thus warm-ion cases with $\rho_s > 0.01a$ have a reduced saturation amplitude and a smaller total dynamo emf at saturation relative to resistive MHD.

As emphasized throughout the discussion of the tearing structure, the two-fluid effects mix the phases of the perturbations compared to a single-fluid model. Figure 21 shows that Eq. (10) is still a good approximation for the gyroviscous force in the saturated state. As the Laplacian operator does not mix the phases, the stabilizing ion-gyroviscous

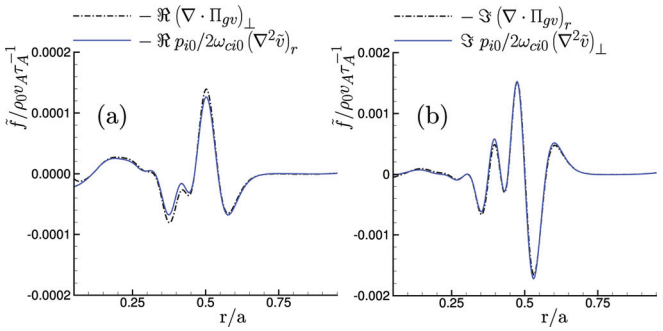

FIG. 21. (Color online) The perpendicular, (a), and radial, (b), ion-gyroviscous stress as well as the leading order terms expressed in Eq. (10) for a computation of the saturated island with $S = 8 \times 10^4$, $\beta = 0.1$, $\rho_s = 0.05a$ and warm ions.

force in phase with the reconnecting flow, such as in Fig. 20, is out of phase with the flow eddy that produces it. Figures 17(b) and 17(d) demonstrate that the dominant ion eddies are out of phase with the reconnecting flows with warm ions. Thus the force balance out of phase with the reconnecting flow is significant. These flow eddies are produced by the interaction of the ion-gyroviscous force produced by the ion flow in phase with reconnection and the Lorentz forces related to the decoupling, where the perturbations have the phases ($\Im\tilde{B}_r$, $\Re\tilde{B}_\perp$) and ($\Im\tilde{J}_r$, $\Re\tilde{J}_\perp$). Figures 13, 15, and 16 show that the perturbations with these phases are nonzero in the warm-ion saturated state.

VI. CONCLUSION

Our computations demonstrate that first-order FLR effects such as ion–electron decoupling and ion gyroviscosity impact tearing mode dynamics at parameters that are relevant to RFP experiments. With warm ions, linear modes are modified by a drift from the gyroviscous stress that is associated with the gradient and poloidal curvature of the magnetic field. The growth rate of the tearing mode is reduced in an intermediate drift regime where $\omega_{*gv} \geq \gamma$, which occurs at lower-ρ_s values than the transition from the collisional regime to the semi-collisional regime for the electron response. These ω_{*gv}-drift contributions are much larger in pinch profiles than they are in large aspect-ratio tokamaks, where curvature and the variation of ion gyrofrequency are weaker. In the large-ρ_s regime, the decoupled electron fluid governs the dynamics of the mode, and our numerical results show that the cold- and warm-ion cases approach the same growth rate for $\rho_s > \delta$. Therefore, the modeling of ion dynamics is less important where ρ_s is largest, and the first-order ion FLR modeling should provide a reasonably good approximation over the entire parameter range.

In the nonlinear regime for these conditions, the island width and characteristic scale lengths are significantly larger than ρ_s, so first-order modeling is well justified. With warm ions, the nonlinear gyroviscous force supplements the perturbed nonlinear Lorentz force and reduces the island saturation width. This contrasts with our cold-ion results and with previous drift-tearing studies for large-island evolution with diamagnetic drift.[17–19] The curvature and gradient of the magnetic field are not greatly modified by the nonlinear island evolution, so the gyroviscous-drift effects are also relatively unchanged, unlike the pressure gradient that is important for diamagnetic-drift effects. Additionally, because the gyroviscous forces balance Lorentz forces, the Hall terms remain significant with warm ions, unlike the results computed for cold ions. With warm ions, the ion flows are substantially distorted by the gyroviscous stress, and the dominant eddy is out of phase with the flow responsible for reconnection.

Our linear and nonlinear single-helicity cases do not represent the dynamic relaxation events observed in RFPs, which result from strong nonlinear interaction among tearing perturbations of multiple resonant helicities. However, because ion and electron temperatures are comparable in the experiment, we expect that the ω_{*gv} drift influences island widths, possibly reducing the mode coupling and magnetic stochasticity that occurs during relaxation events. An experimental measurement of the relative phase between the magnetic perturbation and the ion flow could be compared to the predicted phases from this study in order to empirically determine the importance of the ω_{*gv} drift to a particular discharge.

Our findings may have more direct relevance to RFP discharges achieving QSH and to profile-control experiments.[23,24] As ion temperature increases with improved confinement, it may lead to a self-reinforcing process where the ω_{*gv} drift increases, further limiting the magnetic perturbations. Additionally, QSH discharges are often associated with the dominance of the innermost resonant mode, and we note the poloidal curvature and the gradient of the magnetic field are relatively weak near the magnetic axis. Other modes would be subject to a larger drift effect, so there may be a natural tendency to produce QSH. Further study with the FLR model is needed to clarify the influence of the ω_{*gv} drift effects on these improved confinement discharges and in standard multihelicity RFP dynamics.

ACKNOWLEDGMENTS

The authors would like to thank Professor Chris Hegna and Professor Dalton Schnack for stimulating discussions. This work is supported by the U.S. Department of Energy grants DE-FC02-08ER54975 and DE-FG02-06ER54850 and by National Science Foundation grant PHY-0821899. Computations were performed at the National Energy Research Scientific Computing Center, which is supported by the Office of Science of the U.S. Department of Energy under Contract No. DE-AC02-05CH11231.

APPENDIX: GYROVISCOUS TENSOR CALCULATIONS

Our heuristic linear model considers the effect of nearly incompressible flows represented by a steam function, $\tilde{\mathbf{v}} = \hat{\mathbf{b}} \times \nabla\tilde{\phi}$, orders radial derivatives of $\tilde{\phi}$ as ϵ^{-1}, and makes Taylor expansions of the axisymmetric quantities in $x = r - r_s$, where $|x|$ is of order ϵ. All other quantities, including the wavenumber k, are of order ϵ^0. Thus, we may write

$$\hat{\mathbf{b}} \to \hat{\mathbf{b}}_s + x\hat{\mathbf{b}}'_s + \frac{1}{2}x^2\hat{\mathbf{b}}''_s + \cdots, \tag{A1}$$

$$\mathbf{k} \to \mathbf{k}_s + x\mathbf{k}'_s + \frac{1}{2}x^2\mathbf{k}''_s + \cdots, \tag{A2}$$

$$\frac{1}{r_s} \to \frac{1}{r_s} - \frac{x}{r_s^2} + \frac{x^2}{r_s^3} + \cdots, \tag{A3}$$

where the subscript s indicates evaluation at the resonant surface and $k_{\|s} = \hat{\mathbf{b}}_s \cdot \mathbf{k}_s = 0$. Dropping the subscript s, we write the cylindrical ordered operators

$$\nabla\phi \to \underbrace{\phi'\hat{r}}_{\sim\epsilon^{-1}} + \underbrace{i\mathbf{k}\phi}_{\sim\epsilon^0} + \underbrace{i\mathbf{k}'x\phi}_{\sim\epsilon} + \underbrace{\frac{i\mathbf{k}'^2}{2}\phi}_{\sim\epsilon^2} + \mathcal{O}(\epsilon^3), \tag{A4}$$

$$\nabla \mathbf{v} \rightarrow \underbrace{\sum_j v_j' \hat{r}\hat{e}_j}_{\sim\epsilon^{-1}} + \underbrace{i\mathbf{k}\mathbf{v} + \frac{1}{r}\left(v_r \hat{\theta}\hat{\theta} - v_\theta \hat{\theta}\hat{r}\right)}_{\sim\epsilon^0} + \underbrace{ix\mathbf{k}'\mathbf{v} - \frac{x}{r^2}\left(v_r \hat{\theta}\hat{\theta} - v_\theta \hat{\theta}\hat{r}\right)}_{\sim\epsilon} + \mathcal{O}(\epsilon^2), \tag{A5}$$

$$(\nabla \cdot \mathbf{T})_r \rightarrow \underbrace{T_{rr}'}_{\sim\epsilon^{-1}} + \underbrace{(i\mathbf{k}\cdot\mathbf{T})_r + \frac{1}{r}(T_{rr} - T_{\theta\theta})}_{\sim\epsilon^0} + \underbrace{(i\mathbf{k}'x\cdot\mathbf{T})_r - \frac{x}{r^2}(T_{rr} - T_{\theta\theta})}_{\sim\epsilon} + \mathcal{O}(\epsilon^2), \tag{A6}$$

$$(\nabla \cdot \mathbf{T})_\theta \rightarrow \underbrace{T_{r\theta}'}_{\sim\epsilon^{-1}} + \underbrace{(i\mathbf{k}\cdot\mathbf{T})_\theta + \frac{1}{r}(T_{r\theta} + T_{\theta r})}_{\sim\epsilon^0} + \underbrace{(i\mathbf{k}'x\cdot\mathbf{T})_\theta - \frac{x}{r^2}(T_{r\theta} + T_{\theta r})}_{\sim\epsilon} + \mathcal{O}(\epsilon^2), \tag{A7}$$

$$(\nabla \cdot \mathbf{T})_z \rightarrow \underbrace{T_{rz}'}_{\sim\epsilon^{-1}} + \underbrace{(i\mathbf{k}\cdot\mathbf{T})_z}_{\sim\epsilon^0} + \underbrace{(i\mathbf{k}'x\cdot\mathbf{T})_z}_{\sim\epsilon} + \mathcal{O}(\epsilon^2), \tag{A8}$$

$$\hat{\mathbf{b}}\cdot\nabla\times\mathbf{A} \rightarrow \underbrace{b_z A_\theta' - b_\theta A_z'}_{\sim\epsilon^{-1}} \underbrace{- ikA_r + b_z\frac{A_\theta}{r} + x\left(b_z' A_\theta' - b_\theta' A_z'\right)}_{\sim\epsilon^0} \underbrace{- ik'xA_r + xb_z'\frac{A_\theta}{r} + \frac{x^2}{2}\left(b_z'' A_\theta' - b_\theta'' A_z'\right)}_{\sim\epsilon} + \mathcal{O}(\epsilon^2), \tag{A9}$$

where the order of the operator, not the result, is indicated.

The gyroviscous force contains at most three radial derivatives from differential operations: the divergence of Π, the $\nabla\tilde{\mathbf{v}}$ in the rate of strain tensor, and the gradient of $\tilde{\phi}$. Thus, the gyroviscous force has lowest-order terms at ϵ^{-3} and is given to $\mathcal{O}(\epsilon^{-2})$ in Eq. (8). For the parallel ion-gyroviscous torque, the radial derivatives in the curl operation act only on the perpendicular force, which is of $\mathcal{O}(\epsilon^{-2})$, so there is no contribution to the torque at $\mathcal{O}(\epsilon^{-4})$. In fact, as discussed in Sec. IV A, the radial derivative of the lowest-order perpendicular force, $\mathcal{O}(\epsilon^{-2})$, cancels exactly with the $\mathcal{O}(\epsilon^{-3})$ term $ik(\nabla\cdot\Pi)_r$ from the radial force during the curl operation. This cancellation is related to the nearly incompressible nature of the flows, and thus there are at most terms of $\mathcal{O}(\epsilon^{-2})$ in the gyroviscous torque. This requires evaluation of the perpendicular gyroviscous force to $\mathcal{O}(\epsilon^{-1})$, where the additional terms at $\mathcal{O}(\epsilon^{-1})$ are

$$\frac{p_{i0}}{2\omega_{ci0}}\left[ik_\perp'\left(3\tilde{\phi}' + x\tilde{\phi}''\right) + \frac{4ik_\perp\tilde{\phi}'}{r}\left(1 - \frac{b_\theta^2}{2}\right)\right] + \left(\frac{p_{i0}}{2\omega_{ci0}}\right)' ik_\perp\left[2\tilde{\phi}' + x\tilde{\phi}''\right]. \tag{A10}$$

Applying the $\hat{\mathbf{b}}\cdot\nabla\times$ operation to the gyroviscous forces through $\mathcal{O}(\epsilon^{-1})$, we find the $\mathcal{O}(\epsilon^{-2})$ gyroviscous torque, Eq. (11). This result has been confirmed with a Mathematica computation.

[1] H. P. Furth, J. Killeen, and M. N. Rosenbluth, Phys. Fluids **6**, 459 (1963).
[2] J. A. Holmes, B. A. Carreras, P. H. Diamond, and V. E. Lynch, Phys. Fluids **31**(5), 1166 (1988).
[3] Y. L. Ho and G. G. Craddock, Phys. Fluids **3**(3), 030721 (1991).
[4] H. K. Moffatt, *Magnetic Field Generation in Electrically Conducting Fluids* (Cambridge University Press, Cambridge, 1978).
[5] D. D. Schnack, E. J. Caramana, and R. A. Nebel, Phys. Fluids **28**(1), 321 (1985).
[6] V. V. Mirnov, C. C. Hegna, and S. C. Prager, Plasma Phys. Rep. **29**(7), 566 (2003).
[7] R. Nebel, in Proceedings of the Physics of Alternative Magnetic Confinement Schemes edited by S. Ortoloni and E. Sindoni (Societa Italiana di Fisica, Editrice Compositori, Bologna, Italy, 1991), p. 611.
[8] R. N. Dexter, D. W. Kerst, T. W. Lovell, S. C. Prager, and J. C. Sprott, Fusion Technol. **19**, 131 (1991).
[9] W. X. Ding, D. L. Brower, D. Craig, B. H. Deng, G. Fiksel, V. V. Mirnov, S. C. Prager, J. S. Sarff, and V. Svidzinski, Phys. Rev. Lett. **93**(4), 045002 (2004).
[10] A. Kuritsyn, G. Fiksel, A. F. Almagri, D. L. Brower, W. X. Ding, M. C. Miller, V. V. Mirnov, S. C. Prager, and J. S. Sarff, Phys. Plasmas **16**, 055903 (2009).
[11] B. Coppi, Phys. Fluids **7**, 1501 (1964).
[12] J. F. Drake and Y. C. Lee, Phys. Fluids **20**(8), 1341 (1977).
[13] L. Zakharov and B. Rogers, Phys. Fluids B **4**(10), 3285 (1992).
[14] B. N. Rogers, R. E. Denton, J. F. Drake, and M. A. Shay, Phys. Rev. Lett. **87**(19), 195004 (2001).
[15] V. V. Mirnov, C. C. Hegna, and S. C. Prager, Phys. Plasmas **11**(9), 4468 (2004).
[16] E. Ahedo and J. J. Ramos, Plasma Phys. Controlled Fusion **51**, 055018 (2009).
[17] D. Biskamp, Nucl. Fusion **19**(6), 777 (1979).
[18] D. A. Monticello and R. B. White, Phys. Fluids **23**(2), 366 (1980).
[19] B. D. Scott, J. F. Drake, and A. B. Hassam, Phys. Rev. Lett. **54**(10), 1027 (1985).
[20] P. H. Rutherford, Phys. Fluids **16**(11), 1903 (1973).
[21] J. F. Drake, T. M. Antonsen, Jr., A. B. Hassam, and N. T. Gladd, Phys. Fluids **26**(9), 2509 (1983).
[22] B. D. Scott and A. B. Hassam, Phys. Fluids **30**(1), 90 (1987).
[23] P. Martin, L. Marrelli, G. Spizzo, P. Franz, P. Piovesan, I. Predebon, T. Bolzonella, S. Cappello, A. Cravotta, D. F. Escande, L. Frassinetti, S. Ortolani, R. Paccagnella, D. Terranova, the RFX team, B. E. Chapman, D. Craig, S. C. Prager, J. S. Sarff, the MST team, P. Brunsell, J.-A. Malmberg, J. Drake, the EXTRAP T2R team, Y. Yagi, H. Koguchi, Y. Hirano, the TPE-RX team, R. B. White, C. Sovinec, C. Xiao, R. A. Nebel, and D. D. Schnack, Nucl. Fusion **43**(12), 1855 (2003).
[24] J. S. Sarff, A. F. Almagri, J. K. Anderson, T. M. Biewer, A. P. Blair, M. Cengher, B. E. Chapman, P. K. Chattopadhyay, D. Craig, D. J. D. Hartog,

F. Ebrahimi, G. Fiksel, C. B. Forest, J. A. Goetz, D. Holly, B. Hudson, T. W. Lovell, K. J. McCollam, P. D. Nonn, R. O'Connell, S. P. Oliva, S. C. Prager, J. C. Reardon, M. A. Thomas, M. D. Wyman, D. L. Brower, W. X. Ding, S. D. Terry, M. D. Carter, V. I. Davydenko, A. A. Ivanov, R. W. Harvey, R. I. Pinsker, and C. Xiao, Nucl. Fusion, **43**(12), 1684 (2003).
[25]A. N. Kaufman, Phys. Fluids **3**(4), 610 (1960).
[26]S. I. Braginskii, "Transport properties in a plasma," in *Rev. Plasma Phys*., edited by M. A. Leontovish (Consultants Bureau, New York, 1965), Vol. 1, pp. 205–311.
[27]J. F. Drake and Y. C. Lee, Phys. Rev. Lett. **39**(8), 453 (1977).
[28]C. R. Sovinec, A. H. Glasser, T. A. Gianakon, D. C. Barnes, R. A. Nebel, S. E. Kruger, D. D. Schnack, and S. J. Plimpton, J. Comput. Phys. **195**, 355 (2004).
[29]C. R. Sovinec, J. R. King, and the NIMROD Team, J. Comput. Phys. **229**, 5803 (2010).
[30]P. Zhu, D. D. Schnack, F. Ebrahimi, E. G. Zweibel, M. Suzuki, C. C. Hegna, and C. R. Sovinec, Phys. Rev. Lett. **101**(8), 085005 (2008).
[31]D. C. Robinson, Nucl. Fusion, **18**, 939 (1978).
[32]R. D. Hazeltine and J. D. Meiss, *Plasma Confinement* (Dover, New York, 2003).
[33]B. Coppi, J. M. Green, and J. L. Johnson, Nucl. Fusion **6**, 101 (1966).
[34]D. Bonfiglio, S. Cappello, and D. F. Escande, Phys. Rev. Lett. **94**(14), 145001 (2005).
[35]S. Cappello, D. Bonfiglio, and D. F. Escande, Phys. Plasmas **13**(5), 056102 (2006).